The Astrophysical Journal, 931:36 (10pp), 2022 May 20 https://doi.org/10.3847/1538-4357/ac66e1


# Ion Acoustic Shock Wave Formation and Ion Acceleration in the Interactions of Pair Jets with Electron–ion Plasmas

Jian Huang[1,2], Su-Ming Weng[1,2], Xin Wang[3], Jia-Yong Zhong[4], Xing-Long Zhu[1,2,5], Xiao-Feng Li[1,2], Min Chen[1,2], Masakatsu Murakami[6], and Zheng-Ming Sheng[1,2,5,7]

[1] Key Laboratory for Laser Plasmas (MoE), School of Physics and Astronomy, Shanghai Jiao Tong University, Shanghai 200240, People's Republic of China wengsuming@sjtu.edu.cn
[2] Collaborative Innovation Center of IFSA, Shanghai Jiao Tong University, Shanghai 200240, People's Republic of China; zmsheng@sjtu.edu.cn
[3] Xinjiang Astronomical Observatory, Chinese Academy of Sciences, Urumqi 830011, People's Republic of China
[4] Department of Astronomy, Beijing Normal University, Beijing 100875, People's Republic of China
[5] Tsung-Dao Lee Institute, Shanghai Jiao Tong University, Shanghai 200240, People's Republic of China
[6] Institute of Laser Engineering, Osaka University, Osaka 565-0871, Japan
[7] SUPA, Department of Physics, University of Strathclyde, Glasgow G4 0NG, UK
*Received 2022 January 21; revised 2022 April 10; accepted 2022 April 11; published 2022 May 23*

## Abstract

Astrophysical jets are ubiquitous in the universe and often associated with compact objects, and their interactions with the ambient medium not only dissipate their own energy but also provide ideal circumstances for particle acceleration. By means of theoretical analysis and particle-in-cell simulations, here we study the ion acoustic shock wave (IASW) formation and consequent ion acceleration when electron–positron ($e^-e^+$) jets are injected into ambient electron–ion plasmas. It is found that the Buneman instability can be excited first, which induces the formation of an ion acoustic wave (IAW). As the amplitude of the IAW increases, its waveform is steepened and subsequently an IASW is formed. Some ions in the ambient plasmas will be reflected when they encounter the IASW, and thus can be accelerated to form an energetic ion beam. For an initial $e^-e^+$ jet with the Lorentz factor $\gamma_0 = 100$ and the ion–electron mass ratio $m_i/m_e = 1836$, the ions can be accelerated up to 580 MeV. This study deepens our understanding of the fireball model of gamma-ray bursts, the shock model of pulsar wind nebulae, the origin of cosmic rays, and other related astrophysical processes.

*Unified Astronomy Thesaurus concepts:* Shocks (2086); Jets (870); Gamma-ray bursts (629); Plasma astrophysics (1261); Cosmic ray astronomy (324)

## 1. Introduction

The astrophysical jets are tightly collimated, high-speed outflows of plasmas that are associated with active galactic nuclei (AGN) (Perry & Dyson 1985; Romero et al. 2017; Blandford et al. 2019; Polkas et al. 2021), gamma-ray bursts (GRBs) (Piran 2004; Zhang 2018), X-ray binaries (XRBs) (Migliari & Fender 2006; Russell et al. 2013), quasars and microquasars (Wardle et al. 1998; Abeysekara et al. 2018), blazars (Hovatta & Lindfors 2019), and black holes and other compact objects (Mirabel & Rodríguez 1999; Liu et al. 2007; Belloni 2010). The compositions of the jets are dependent on the circumstances of the sources and the energy release mechanisms in the corresponding astrophysical scenarios. They are mostly made up of ions and electrons, electron–positron ($e^-e^+$) pairs, or a mixture of both. As the most luminous ($\sim 10^{51}$–$10^{53}$ erg s$^{-1}$) explosions in the universe, GRBs are capable of releasing an enormous amount of energy in a small volume of radius $\sim 10^3$ km, in which a huge amount of $e^-e^+$ pairs may be produced. And then the produced pair jet propagates into an ambient plasma that is made of baryonic matter (Piran 2004; Zhang 2018). The polarization properties of the core regions of quasar 3C 279 and 3C 345 show that the jet plasmas are usually dominated by $e^-e^+$ pairs (Wardle et al. 1998; Sikora & Madejski 2000; Hirotani et al. 2000), and may also contain a portion of protons (Homan et al. 2009). According to the jet speed, the jets can be divided into relativistic jets and nonrelativistic jets. For relativistic jets, most of them are located in extragalactic sources and very far away from the earth, and their fundamental properties are still very poorly understood. Relativistic shocks generated in pair plasmas have been identified as one of the major sources of particle acceleration and high-energy electromagnetic radiation in several classes of astrophysical objects. Astronomical observations of jets are mainly based on the radiation properties of energetic particles accelerated by relativistic shocks associated with jets through synchrotron radiation, Compton processes, or other radiation mechanisms. The study of the complex radiative features of relativistic jets is the main way to gain an insight into jet physical conditions.

The shock excitation and subsequent particle acceleration in the interactions of jets with the ambient mediums were studied extensively on many different scales. Using analytic and numerical methods, Blandford & Rees (1974) and Scheuer (1974) showed that the jets can generate a bow shock structure and emit radio radiation when they impinge on an intergalactic medium. Recent large-scale numerical simulations with particle-in-cell (PIC) codes have provided new insights into the microphysics of jet dynamics and particle acceleration, such as how and where in the jets the particles are accelerated. For example, Nishikawa et al. (2003) discovered that a collisionless shock can be excited by the Weibel instability (Weibel 1959) behind the front of an electron–proton jet, and the excited shock can accelerate the particles in both the perpendicular and parallel directions to the jet propagation direction. More

recently, Nishikawa et al. (2020) also found that the helical magnetic field can affect the kinetic instabilities and it will also become turbulent due to reconnection-like phenomena, where the electrons can be repeatedly accelerated as they encounter the magnetic reconnection events in the turbulent magnetic field. Cui et al. (2015) investigated the interaction of a high-energy lepton flow with an ambient electron–ion plasma and found a two-stage acceleration of the ambient ions. First, the ions are accelerated by the turbulent magnetic field islands generated via the Weibel-type instabilities and form a globally inverse-power energy spectrum. Second, a shock wave front forms in the ambient plasma, which further accelerates the ambient ions to energy higher than that gained in the first stage. Sinha et al. (2019) and Sinha & Kumar (2020) studied the polarized radiation generation from a charge-neutral $e^-e^+$ beam propagating in a magnetized ambient electron–proton plasma, where the presence of a strong magnetic field enables ultrarelativistic particles to emit synchrotron radiation. Relativistic shocks in pair plasmas have been extensively studied, and significant progress has been made in the understanding of the underlying physical mechanisms of particle acceleration and high-energy radiation (Langdon et al. 1988; Spitkovsky 2008; Plotnikov & Sironi 2019; Sironi et al. 2021). Since magnetic fields are also often embedded in astrophysical pair jets (Reynolds et al. 1996; Homan et al. 2009), the study of magnetized pair jets, especially their difference from electron–ion plasmas, is critical to making sense of some astrophysical observations. The particle acceleration and turbulence in magnetized pair plasmas have been widely investigated (Langdon et al. 1988; Gallant et al. 1992; Saito & Sakai 2004; Amato & Arons 2006; Sironi et al. 2013; Loureiro & Boldyrev 2018). The effect of magnetic field on the collisionless shock formation and particle acceleration in relativistic pair plasmas has been studied by Sironi & Spitkovsky (2009), and it is found that the efficient particle acceleration exists only for a very small range of the inclination angles between the preshock magnetic field and the shock normal. Plotnikov et al. (2018) have found that the structure of perpendicular relativistic shocks will change from Weibel-dominated to magnetic-reflection-shaped shocks with the increasing magnetization of pair plasmas, and the particle acceleration is efficient in weakly magnetized perpendicular shocks.

In this paper, we study the ion acceleration by the ion acoustic shock waves (IASW) (Popel et al. 1995; Shah & Saeed 2009; Kakad et al. 2013; Kakad & Kakad 2016; Lotekar et al. 2017) that are generated when the $e^-e^+$ jets are injected into the ambient electron–ion plasmas. This scenario may be related to some physical processes in astrophysical objects, such as the pulsar wind nebula (PWN) shock systems (van der Swaluw et al. 2003) and the fireball model of GRBs (Piran 2004; Waxman 2006). We find that the formation process of IASW consists of two steps. First, an ion acoustic wave (IAW) is generated due to the Buneman instability (Buneman 1958, 1959) when the $e^-e^+$ jet is injected into the ambient electron–ion plasma. Second, the IAW will further evolve into an IASW when the Buneman instability is dominated by nonlinear effects. As the IASW moves toward the upstream plasma at a high speed, some ions in the upstream ambient plasma can be reflected and accelerated by the IASW to form a quasi-monoenergetic ion beam.

For the sake of simplicity, in this study we will restrict the discussion to one-dimensional (1D) PIC simulations and focus on the basic aspects of the IASW formation and ion acceleration. The paper is organized as follows. First, we will derive the conditions for the generation of IAWs that are mediated by the Buneman instability in the interactions of the $e^-e^+$ jets with the ambient electron–ion plasmas. Second, the formations of both the IAWs and the IASWs will be described in detail. Finally, the ion acceleration by the IASW and the energy spectrum of the accelerated ion beam will be analyzed, and the robustness of the IASW formation and ion acceleration will also be discussed.

**Table 1**
Notations of the $e^-e^+$ Jet and Ambient Plasma Parameters

| | Initial Velocity | Perturbation Velocity | Initial Density | Perturbation Density |
|---|---|---|---|---|
| jet electron | $v_0$ | $v_{ej1}$ | $n_j$ | $n_{ej1}$ |
| jet positron | $v_0$ | $v_{p1}$ | $n_j$ | $n_{p1}$ |
| ambient electron | 0 | $v_{e_{am}1}$ | $n_{am}$ | $n_{e_{am}1}$ |
| ambient ion | 0 | $v_{i1}$ | $n_{am}$ | $n_{i1}$ |

## 2. Theory of Buneman Instability in Jets

First we derive the dispersion relation of the Buneman instability (Buneman 1958, 1959; Dieckmann et al. 2000; Lemoine & Pelletier 2011; Guo & Yu 2012) that develops when an $e^-e^+$ jet interacts with an ambient electron–ion plasma. The Buneman instability can be induced by an energetic particle stream that is injected into a plasma, or by setting a current along the plasma where different particle species (ions, electrons, or positrons) will have different drift velocities. In plasmas, the natural oscillation frequency of the electron fluid is $\omega_{pe} = (n_0 e^2/\epsilon_0 m_e)^{1/2}$, while the natural oscillation frequency of the ion fluid is $\Omega_p = (m_e/m_i)^{1/2}\omega_{pe}$, where $n_0$ is the number density of plasma, $m_e$ and $m_i$ are the masses of electrons (or positrons) and ions, respectively. Due to the Doppler frequency shift of the electron oscillation in the moving electron fluid, however, these two frequencies can coincide in the laboratory frame if the velocities of the two fluids are proper. Consequently, the Buneman instability can be excited (Chen 2016).

The notations of the $e^-e^+$ jet and ambient plasma parameters are displayed in Table 1, where the subscripts "0" and "1" denote the background and perturbed quantities, respectively. The jet electron velocity is $\boldsymbol{v}_{e_j} = \boldsymbol{v}_0 + \boldsymbol{v}_{ej1}$, the jet electron density is $n_{e_j} = n_j + n_{ej1}$, the jet positron velocity is $\boldsymbol{v}_p = \boldsymbol{v}_0 + \boldsymbol{v}_{p1}$, the jet positron density is $n_p = n_j + n_{p1}$, the ambient electron velocity is $\boldsymbol{v}_{e_{am}} = \boldsymbol{v}_{e_{am}1}$, the ambient electron density is $n_{e_{am}} = n_{am} + n_{e_{am}1}$, the ambient ion velocity is $\boldsymbol{v}_i = \boldsymbol{v}_{i1}$, and the ambient ion density is $n_i = n_{am} + n_{i1}$.

The motion and continuity equations of different particle species are generally given by:

$$m_s n_s \left[\frac{\partial \boldsymbol{v}_s}{\partial t} + (\boldsymbol{v}_s \cdot \nabla)\boldsymbol{v}_s\right] = q_s n_s E, \quad (1)$$

$$\frac{\partial n_s}{\partial t} + \nabla \cdot (n_s \boldsymbol{v}_s) = 0, \quad (2)$$

for $s = e_j$, $p$, $e_{am}$, $i$ represents jet electrons, jet positrons, ambient electrons, and ambient ions, respectively. And the

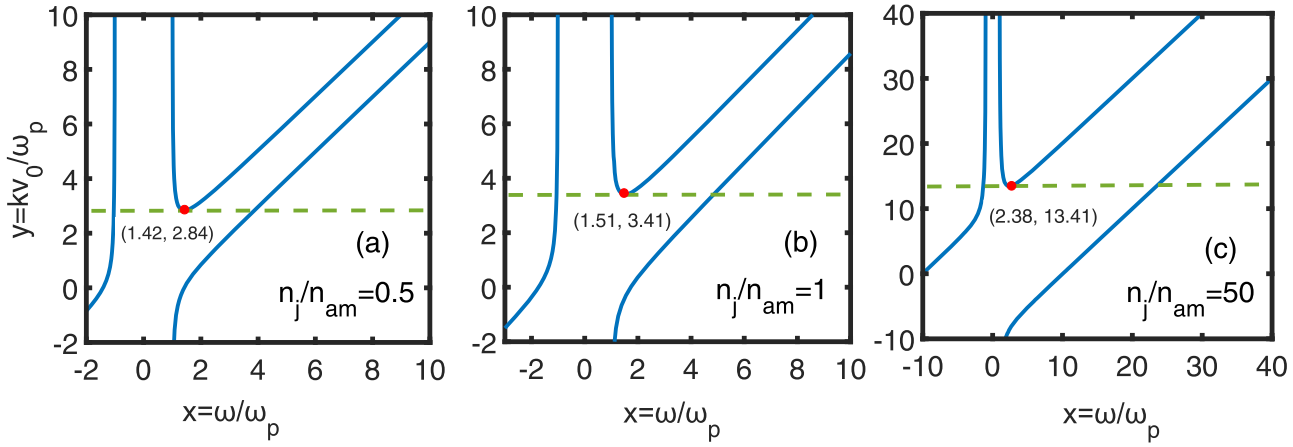


**Figure 1.** Dispersion relation of the Buneman instability in the interaction of an $e^{-}e^{+}$ jet with an ambient electron–ion plasma, where the plasma density ratios are (a) $n_j/n_{\rm am} = 0.5$, (b) $n_j/n_{\rm am} = 1$, and (c) $n_j/n_{\rm am} = 50$, respectively. The dashed line gives the threshold wavevector for the instability. When $y = kv_0/\omega_p$ is below the dashed line, the Buneman instability can be triggered, which leads to the formation of IAW.

electric field is related to the densities by Poisson's equation

$$\epsilon_0 \nabla \cdot E = \sum_s n_s q_s. \tag{3}$$

We look for an electrostatic wave solution of the form

$$\boldsymbol{E} = E e^{i(kx-\omega t)}\hat{\boldsymbol{x}}, \tag{4}$$

where $\hat{\boldsymbol{x}}$ is the direction of $\boldsymbol{v}_0$ and $\boldsymbol{k}$ in the case of one dimension, and the subscript $x$ is omitted. From Equation (1), we get

$$v_{e_j1} = \frac{-ieE}{m_e(\omega - v_0 k)}, \tag{5}$$

$$v_{p1} = \frac{ieE}{m_e(\omega - v_0 k)}, \tag{6}$$

$$v_{e_{\rm am}1} = \frac{-ieE}{m_e \omega}, \tag{7}$$

$$v_{i1} = \frac{ieE}{m_i \omega}, \tag{8}$$

substituting Equations (5)–(8) into Equation (2), the perturbation parts of the densities can be obtained

$$n_{e_j1} = \frac{n_j k v_{e_j1}}{\omega - v_0 k} = \frac{-ieEn_j k}{m_e(\omega - v_0 k)^2}, \tag{9}$$

$$n_{p1} = \frac{n_j k v_{p1}}{\omega - v_0 k} = \frac{ieEn_j k}{m_e(\omega - v_0 k)^2}, \tag{10}$$

$$n_{e_{\rm am}1} = \frac{n_{\rm am} k v_{e_{\rm am}1}}{\omega} = \frac{-ieEn_{\rm am} k}{m_e \omega^2}, \tag{11}$$

$$n_{i1} = \frac{n_{\rm am} k v_{i1}}{\omega} = \frac{ieEn_{\rm am} k}{m_i \omega^2}, \tag{12}$$

substituting Equations (9)–(12) into Equation (3), the dispersion relation of the Buneman instability can be obtained (Buneman 1958; Chen 2016)

$$1 = \omega_p^2 \left[ \frac{2(n_j/n_{\rm am})}{(\omega - v_0 k)^2} + \frac{m_e/m_i}{\omega^2} + \frac{1}{\omega^2} \right], \tag{13}$$

where $\omega_p = (n_{\rm am} e^2/\epsilon_0 m_e)^{1/2}$ is the electron plasma frequency of the ambient plasma. Equation (13) is a fourth-order equation for $\omega$. Correspondingly, four roots of $\omega$ may be real or complex, and each real root indicates a possible stable oscillation mode. The complex roots may occur in conjugate pairs, one of which will correspond to an unstable oscillation mode (Chen 2016). Let us define $x = \omega/\omega_p$, $y = kv_0/\omega_p$, then Equation (13) becomes

$$2x^2 + (x - y)^2 (n_{\rm am}/n_j)[(m_e/m_i + 1) - x^2] = 0. \tag{14}$$

Unless otherwise specified, in most simulations we will use the reduced ion-to-electron mass ratio $m_i/m_e = 100$ in order to quicken the simulation and hence save the computation resource. With $m_i/m_e = 100$, the numerical solution of Equation (14) is shown for $n_j/n_{\rm am} = 0.5$, 1, and 50 in Figure 1. The dashed lines in Figure 1 are the separatrices between the unstable and stable regimes. If $y = kv_0/\omega_p$ is below the dashed line, Equations (14) will have two real roots and two complex roots. The two complex roots are conjugate to each other, and one is a damping root while another is an unstable root (growth root), respectively (Chen 2016). That is to say, the plasma becomes unstable and the Buneman instability develops when $kv_0$ is very small. For a constant $v_0$, therefore, the plasma is always unstable to long-wavelength oscillations.

By setting $\partial y/\partial x = 0$ in Equation (14), we can obtain the normalized threshold wavevector ($y_{\rm th} = k_{\rm th} v_0/\omega_p$) of the Buneman instability as

$$y_{\rm th} = \beta^{1/2}[1 + (2\alpha/\beta)^{1/3}]^{3/2} \tag{15}$$

where $\alpha = n_j/n_{\rm am}$ and $\beta = 1 + m_e/m_i$. Correspondingly, $y_{\rm th} = k_{\rm th} v_0/\omega_p$ is achieved at $x_{\rm th} = [\beta + \beta^{2/3}(2\alpha)^{1/3}]^{1/2}$. The normalized threshold wavevector ($y_{\rm th} = k_{\rm th} v_0/\omega_p$) is shown as a function of the plasma density ratio $n_j/n_{\rm am}$ in Figure 2 with $m_i/m_e = 100$. With the increasing $n_j/n_{\rm am}$, both Figures 1 and 2 indicate that the threshold wavevector of the Buneman instability increases. Correspondingly, the threshold wavelength decreases and the plasma becomes more sensitive to the Buneman instability with the increasing $n_j/n_{\rm am}$. It can be seen from the following simulations that the Buneman instability plays an important role in the formation of IAWs.

## 3. Ion Acoustic Waves Formation

Using the code OSIRIS (Fonseca et al. 2002), a series of 1D3V (one dimension in space and three dimensions in

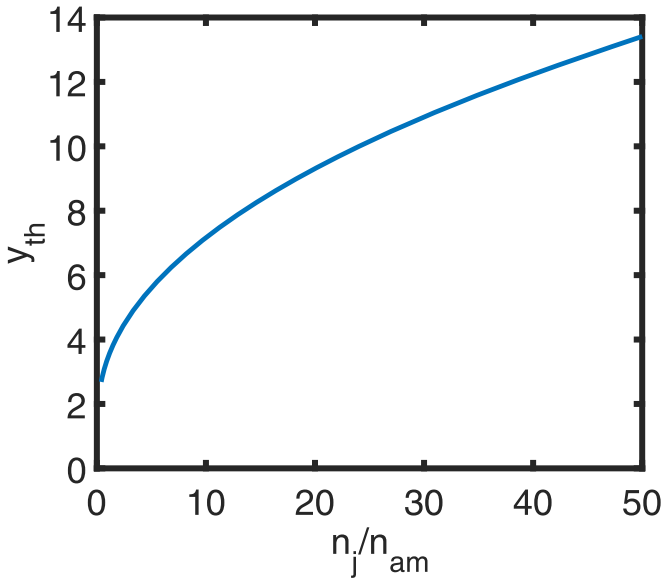


**Figure 2.** The normalized threshold wavevector ($y_{\rm th} = k_{\rm th} v_0/\omega_p$ ) of the Buneman instability as a function of the plasma density ratio $n_j/n_{\rm am}$ obtained from Equation (15), where the ion-to-electron mass ratio is set as $m_i/m_e = 100$.

velocity) PIC simulations are carried out to investigate the interaction of a cold pair jet with a cold ambient electron–ion plasma. The time, length, and electric field are respectively normalized to $\omega_p^{-1}$, $c/\omega_p$ and $m_e\omega_p c/e$, where $c/\omega_p$ is the skin depth of the plasma associated with the plasma density $n_{\rm am}$. In most simulations, the simulation box size is $20{,}000c/\omega_p$ along the x-direction with an open boundary condition, the spatial resolution is $0.1c/\omega_p$, and each particle species is represented by 100 macroparticles per cell. The initial $e^-e^+$ jet is placed on the left half of the simulation box ($-10{,}000\ c/\omega_p \sim 0$), and the ambient electron–ion plasma is placed on the right half of the simulation box ($0 \sim 10{,}000c/\omega_p$). The total simulation time is $10{,}000\omega_p^{-1}$. For comparison, an additional simulation with a larger simulation box size $80{,}000c/\omega_p$ ($-40{,}000\ c/\omega_p \sim 40{,}000c/\omega_p$) and a longer simulation time $40{,}000\omega_p^{-1}$ has been performed.

First, we will verify the formation of the IAW induced by the Buneman instability. The time evolutions of the $e^-e^+$ jet and ambient electron–ion plasma densities are shown in Figure 3, where the initial Lorentz factor of $e^-e^+$ jet is $\gamma_0 = 15$, the ion–electron mass ratio is $m_i/m_e = 100$ and the density ratio of the $e^-e^+$ jet to the ambient plasma is $n_j/n_{\rm am} = 1$. When the $e^-e^+$ jet propagates in the ambient plasma, the jet electrons will repel while the jet positrons will attract the ambient plasma electrons. This will violate the quasi-neutrality of the ambient plasma and cause the generation of an inductive electric field. This inductive electric field, in turn, will perturb the ambient electron density as shown in Figure 3(a) and generates a plasma current to neutralize the external jet (Sinha et al. 2019). Following the perturbation in the ambient plasma electron density, the jet electron density is perturbed as shown in Figure 3(b), and then an electron plasma wave is formed which moves at a high speed. After the formation of the electron plasma wave, the Buneman instability (Buneman 1958, 1959) will transfer the energy from the electron plasma wave to the IAW. Finally, the IAW is formed at around $t = 900\omega_p^{-1}$ as shown in Figure 3(c). The velocity of the IAW at first is about 0.05 c, where c is the speed of light in a vacuum, and the wavelength is about $3.6c/\omega_p$, this IAW is a low-frequency wave. The electrons have high mobility because of their low mass; therefore, they can follow the movement of the ions under the attractive Coulomb force and shield the electric field of the ions.

It should be noted that the jet electron density has two different kinds of peaks as shown in Figure 3(b), where the relatively low peaks coincide with the ambient electron density perturbation while the relatively high peaks have a fixed phase difference with the ambient electron density perturbation. The velocity of the corresponding electron plasma wave is about 0.96 c, and its wavelength is about $6c/\omega_p$.

## 4. Ion Acoustic Shock Wave Formation and Ion Acceleration

We have shown that the IAW can be formed at the time $t \approx 900\omega_p^{-1}$ due to the Buneman instability. If the simulation time is much longer ($t > 2500\omega_p^{-1}$), the amplitude of the IAW will be amplified enormously and the nonlinear effect becomes dominant. The nonlinear effect makes the phase velocity at the peak of the IAW greater than that at the trough of the IAW (Judice et al. 1973; Forslund et al. 1979; Rosenau 1988). Consequently, the IAW becomes steeper gradually, and an IASW is excited finally as shown in Figure 4(b) (Popel et al. 1995; Shah & Saeed 2009; Kakad et al. 2013; Lotekar et al. 2017). At $t = 2600\omega_p^{-1}$, Figure 4(b) shows that the front of the IASW is located at $x \approx 845\ c/\omega_p$, while the head of the jet has already arrived at $x \approx 2600\ c/\omega_p$. It is worth mentioning that the ambient ion and electron density distributions are coupled together before the formation of the IASW as shown in Figure 4(a).

As indicated by Figures 4(b), (c), and 5(a), the IASW moves to the right. In the frame with the IASW, the ambient ions in the upstream will flow toward the IASW. Some ions may be reflected and accelerated by the IASW, which forms a quasi-monoenergetic ion beam as shown in Figure 6. The speed of the IASW is not constant but changes periodically. Because the energy of the IASW is dissipated due to the ion acceleration, the speed and amplitude of the IASW decrease until the ion acceleration pauses. Due to the continuous energy replenishment from the injected $e^-e^+$ jet, however, the speed and amplitude of the IASW will increase again, and then the ion acceleration restarts. In other words, the ion acceleration by the IASW also presents periodically.

Figure 5(a) shows that the IASW has been formed obviously at the time $t = 9000\omega_p^{-1}$, and Figure 6 demonstrates that the upstream ions can be accelerated by this IASW. From the density distributions of the $e^-e^+$ jet and ambient plasma (Figure 5(a)), we can identify the location of the IASW as well as the plasma density ratio between the IASW upstream and downstream regions. The IASW may experience splitting and breaking when its amplitude reaches a threshold, and then it will have two peaks as shown in Figure 5(a). The further simulation shows that these two peaks of the IASW will merge to be a single peak again; this process also presents periodically.

Due to the accumulation of ions at the IASW front, a bipolar electrostatic field will usually be formed around the IASW front (Liu et al. 2016), as shown in the subpanel of Figure 5(a). This bipolar electric field will form a potential barrier. In the reference frame moving with the IASW, therefore, the upstream ions move toward the IASW with initial velocities

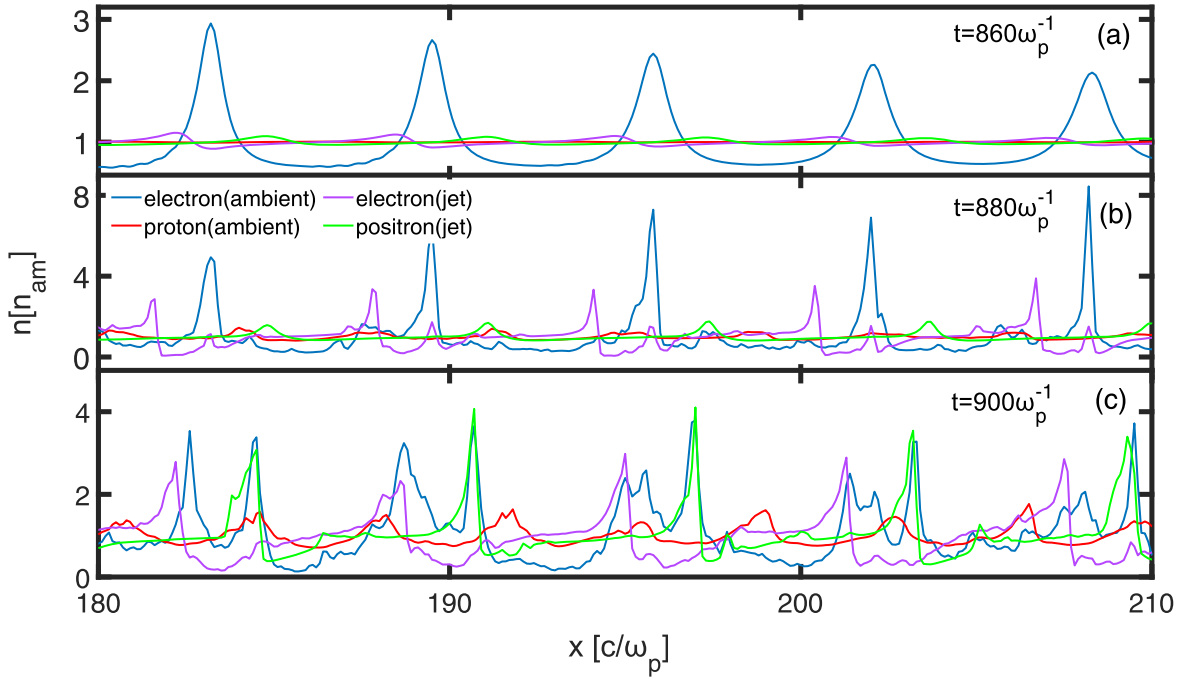


**Figure 3.** The density distributions of the $e^-e^+$ jet and ambient plasma at the simulation time (a) $860\omega_p^{-1}$, (b) $880\omega_p^{-1}$, and (c) $900\omega_p^{-1}$, respectively. The initial Lorentz factor of $e^-e^+$ jet is $\gamma_0 = 15$, the ion–electron mass ratio is $m_i/m_e = 100$, and the density ratio of the $e^-e^+$ jet to the ambient plasma is $n_j/n_{\rm am} = 1$. In the interaction of the $e^-e^+$ jet with an ambient plasma, first the perturbation in the ambient plasma electron density develops as shown in (a), and then the perturbation in the jet electron density develops as shown in (b), and finally the perturbation in the ambient plasma ion density (i.e., IAW) develops as shown in (c).

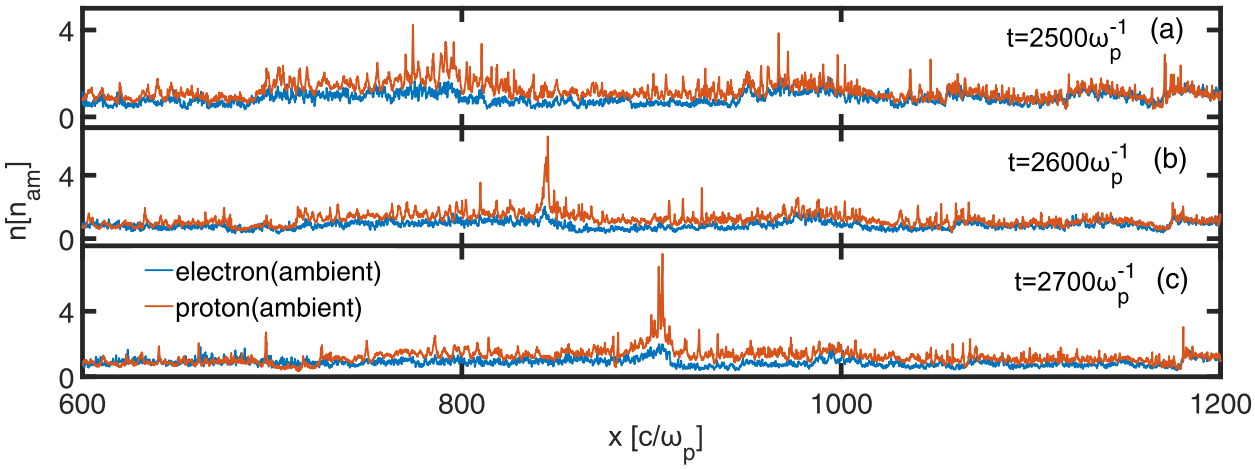


**Figure 4.** The ambient electron and ion density distributions show that the IASW can be formed with the nonlinear evolution of the IAW, the simulation times are (a) $2500\omega_p^{-1}$, (b) $2600\omega_p^{-1}$, and (c) $2700\omega_p^{-1}$, respectively. Other parameters are the same as those in Figure 3.

close to the IASW speed. Some upstream ions will be bounced by the IASW potential barrier and be accelerated if their initial kinetic energy is lower than the IASW potential. In the case of multi IASWs, the electric field will be reversed between the pair of IASWs as shown in the subpanel of Figure 5(a). Therefore, an electrostatic potential well will be formed between two IASW fronts. As a result, some ions may be trapped between the fronts of two IASWs if their kinetic energies are not high enough to overcome the electrostatic potential well. On the other hand, some other ions will be further accelerated by the right IASW if their kinetic energies are high enough to overcome the electrostatic potential well. The trapping or further acceleration of the ions can be identified by the ion momentum distribution near the IASW pair as shown in Figure 5(b). In the upstream and downstream regions far away from the IASW, the jet electrons and the ambient plasma ions are coupled together, and the jet positrons and ambient plasma electrons are coupled together too. Generally speaking, the plasma exhibits a good quasi-neutrality in the region far away from the IASW. The total electron density (jet electron plus ambient plasma electron) in the downstream region is about twice that of the upstream region, and the downstream positron density is also about twice that of the upstream positron density. Because the velocity of the $e^-e^+$ jet is greater than the speed of the IASW, most of the electrons and positrons in the jet will be decelerated when they flow toward the IASW. Conversely, the IASW is driven forward by the jet, consequently the plasma density and temperature rise in the downstream region. A part of the electrons and positrons in the jet may travel through the IASW into the upstream region.

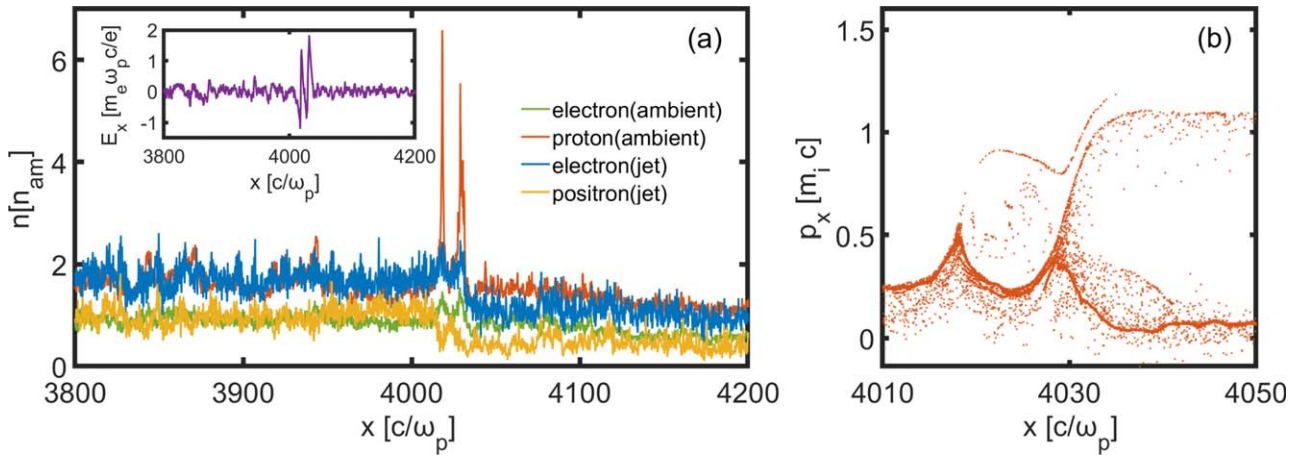


**Figure 5.** Left: the density distributions of the $e^-e^+$ jet and ambient plasma, the subpanel shows the longitudinal electric field. Right: the longitudinal momentum distribution of the ions near the IASW pair. The simulation time is $9000\omega_p^{-1}$, other parameters are the same as those in Figure 3.

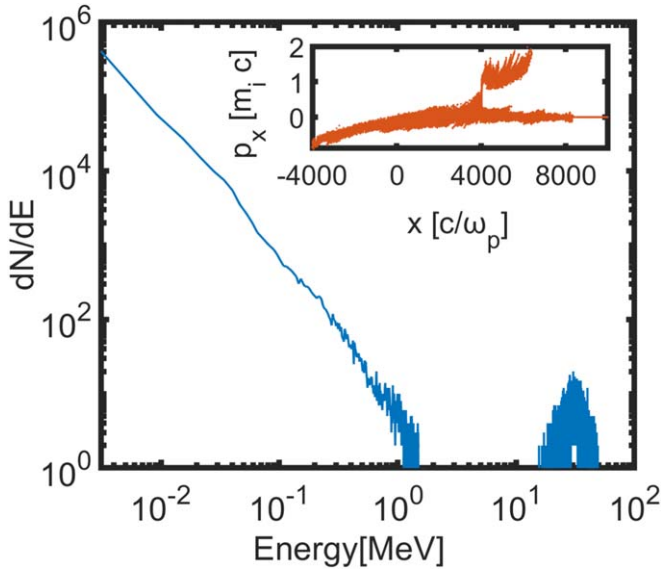


**Figure 6.** Ion energy spectrum in the upstream region $x \geqslant 4030c/\omega_p$ at the time $t = 9000\omega_p^{-1}$. All parameters are the same as those in Figure 3. The subpanel shows the longitudinal momentum distribution of the ions, which also indicates that the IASW locates at $x \approx 4030c/\omega_p$.

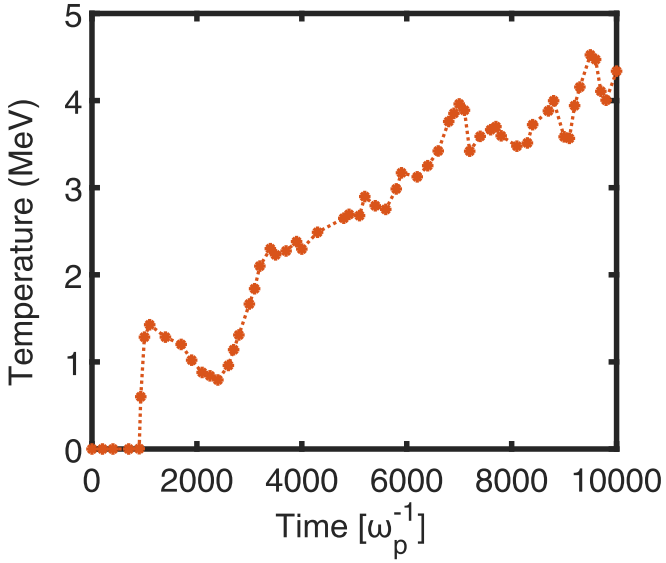


**Figure 7.** Time evolution of the ambient electron temperature around the instantaneous front of the IASW ($\pm 200c/\omega_p$). Before the IASW is formed ($t < 2600\omega_p^{-1}$), the temperature is just averaged around the front of the IASW at the time $t \approx 2600\omega_p^{-1}$.

The longitudinal momentum distribution of the accelerated ions (the subpanel of Figure 6) shows that the IASW is formed at $x \approx 4030c/\omega_p$ at the time $9000\omega_p^{-1}$, which is coincident with Figure 5. Figure 6 displays the energy spectrum of the upstream ions at $x \geqslant 4030c/\omega_p$. It is confirmed that the ions in the ambient plasma are reflected back when they encounter the IASW, forming a quasi-monoenergetic ion beam. The low-energy part of the energy spectrum corresponds to the undisturbed ambient ions in the equilibrium before the arrival of the IASW. With an initial jet velocity $\gamma_0 = 15$ and an artificial ion–electron mass ratio $m_i/m_e = 100$, the spectral peak energy and maximum energies of the ions accelerated by the IASW can reach 31 MeV and 48 MeV, respectively.

The speed of the IASW can also be characterized by the Mach number, defined as $M = v_s/c_s$, where $c_s = (T_e/m_i)^{1/2}$ is the velocity of the IAW and $T_e$ is the electron temperature. We will use the electron average energy to characterize the electron temperature in the simulation. The ambient electron temperature that is spatially averaged around the instantaneous front of the IASW ($\pm 200c/\omega_p$) is shown in Figure 7. It is worth noting that before the IASW is formed ($t < 2600\omega_p^{-1}$), the ambient electron temperature is just averaged around the front of the IASW at the time $t \approx 2600\omega_p^{-1}$. Figure 7 indicates that the ambient electron temperature rises very quickly at the beginning when the $e^-e^+$ jet encounters the ambient plasma, and then it decreases gradually before the IASW is formed. After the IASW is formed, the temperature rises again with some oscillations. At the simulation time $t = 9000\omega_p^{-1}$ (see Figure 5(a)), the temperature of the ambient electrons around the IASW ($\pm 200c/\omega_p$) is about 3.5 MeV, and the corresponding Mach number of the IASW is 1.87.

Both the pair jet and ambient plasma are assumed to be initially cold and nonmagnetized in the above simulations; therefore, their perpendicular temperatures will remain zero during the whole simulation. As a result, only the longitudinal electric field is generated, neither the magnetic field nor the transverse electric field is generated in the above simulations.

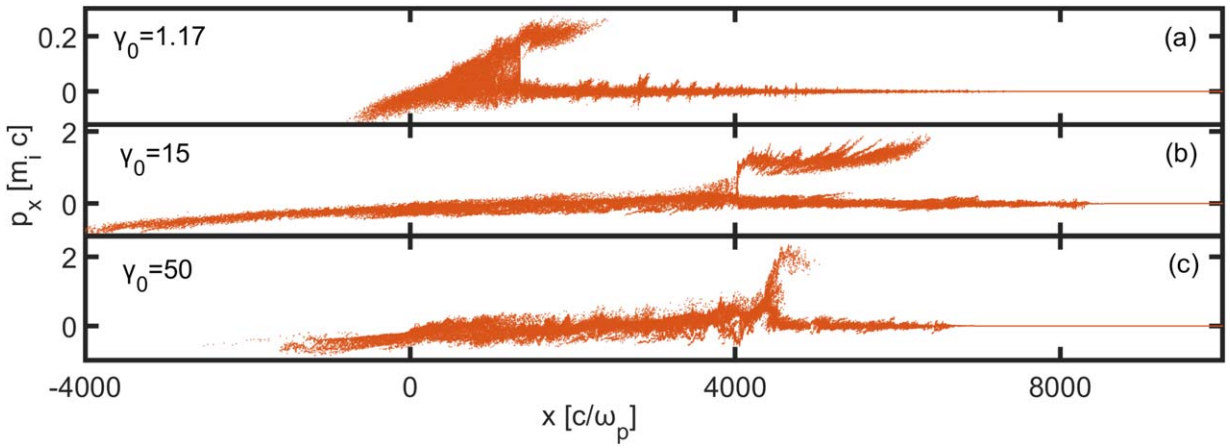


**Figure 8.** The longitudinal momentum distributions of the ions at the time $t = 9000\omega_p^{-1}$ for the different initial jet Lorentz factors: (a) $\gamma_0 = 1.17$, (b) $\gamma_0 = 15$, and (c) $\gamma_0 = 50$, respectively. The ion–electron mass ratio is artificially set as $m_i/m_e = 100$, and the density ratio of the jet to the ambient plasma is fixed as $n_j/n_{\rm am} = 1$.

Consequently, both the IASW formation and the ion acceleration are electrostatic processes in the above simulation cases.

## 5. Parameter Dependence

The robustness of the IASW formation and ion acceleration in the interactions of pair jets with electron–ion plasmas is investigated with a wide range of simulation parameters. For example, the influence of the initial Lorentz factor $\gamma_0$ of the $e^-e^+$ jet is shown in Figures 8 and 9, which indicate that the ions can be accelerated if the initial Lorentz factor of the $e^-e^+$ jet is in the range of $1.17 \leqslant \gamma_0 \leqslant 50$ when the ion–electron mass ratio is $m_i/m_e = 100$ and the density ratio of the jet to the ambient plasma is fixed as $n_j/n_{\rm am} = 1$. If $\gamma_0$ is very small, the energy of the jet will be too low to excite an IASW. With the increase of $\gamma_0$, the IASW begins to form at $\gamma_0 \approx 1.17$, and the ion can be accelerated. With the increase of $\gamma_0$, however, it will take a longer time for the IASW formation. With the increasing $\gamma_0$, the maximum energy of the accelerated ions first increases and reaches its maximum ($\approx$110 MeV) at $\gamma_0 \approx 30$, and then it decreases rapidly. If $\gamma_0$ is too large ($\gamma_0 \geqslant 50$), the IASW cannot be formed since the growth of Buneman instability requires a relatively low $kv_0/\omega_p$ (see Figure 1). Consequently, no obvious ion acceleration is observed.

The influence of the jet and ambient plasma density ratio $n_j/n_{\rm am}$ on the IASW formation and ion acceleration is shown in Figures 10 and 11, which illustrate that the IASW can be formed and the ions can be accelerated effectively in the range of $0.5 \leqslant n_j/n_{\rm am} \leqslant 50$ when the ion–electron mass ratio is $m_i/m_e = 100$ and the initial jet Lorentz factor is fixed as $\gamma_0 = 15$. In the case of a very small plasma density ratio $n_j/n_{\rm am}$, the IASW cannot be formed during the simulation time. This simulation result is consistent with the theoretical analysis in Figures 1 and 2, which show that the threshold wavelength is very short and the plasma becomes insensitive to the Buneman instability for a small $n_j/n_{\rm am}$. With the increasing $n_j/n_{\rm am}$, the IASW begins to form. However, it takes a relatively long time ($t \approx 6500\omega_p^{-1}$) for the IASW formation, and the maximum energy of the accelerated ions is relatively low ($\approx$13 MeV) when $n_j/n_{\rm am} \approx 0.5$. With the further increase of $n_j/n_{\rm am}$, the IASW formation time gets shorter, while the maximum energy of accelerated ions first increases and then remains nearly unchanged ($\approx$63 MeV) in the region $1.5 \leqslant n_j/n_{\rm am} \leqslant 5$. When $n_j/n_{\rm am} \geqslant 5$, the ion maximum energy decreases with the increasing $n_j/n_{\rm am}$. If the plasma density ratio is too large ($n_j/n_{\rm am} > 50$), the IASW will develop very quickly, and more importantly multiple IASWs will be formed and decayed iteratively. Consequently, the structure of the IASWs becomes very complicated, and the accelerated ions will have relatively lower energies with a broader energy spread.

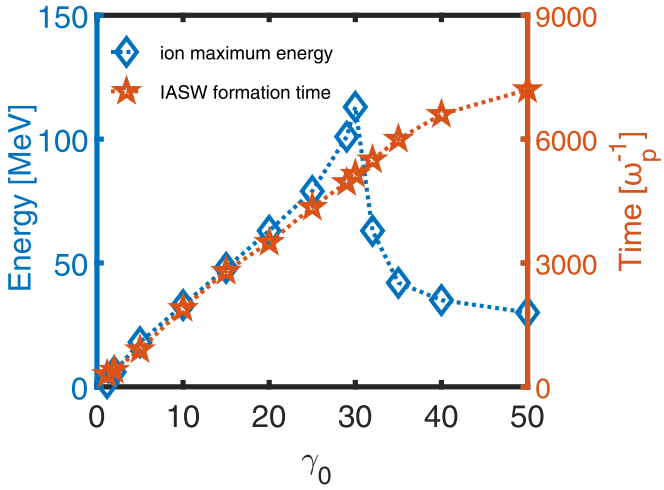


**Figure 9.** The maximum energy of the ions and IASW formation times as a function of the initial $e^-e^+$ jet Lorentz factor $\gamma_0$. Other parameters are the same as those in Figure 8.

The IASW formation and consequent ion acceleration can also take place with the real proton–electron mass ratio $m_i/m_e = 1836$, as shown in Figures 12 and 13, where the initial jet Lorentz factor is $\gamma_0 = 100$ and the jet to the ambient plasma density ratio is $n_j/n_{\rm am} = 1$. The density distributions of the $e^-e^+$ jet and ambient plasma in Figure 12 show that multiple IASWs are formed. The ion energy spectrum in the region $x \geqslant 14{,}000c/\omega_p$ is shown in Figure 13(a), where the maximum energy can reach 580 MeV. It should be noted that this result does not conflict with the result displayed in Figure 8, which indicates that the ISAW cannot be formed if the initial jet Lorentz factor is too fast such as $\gamma_0 = 100$ with an artificial ion–electron mass ratio $m_i/m_e = 100$. In Figures 12 and 13, however, the ion–electron mass ratio is $m_i/m_e = 1836$. It seems that a larger ion–electron mass ratio $m_i/m_e$ will allow a high initial jet Lorentz factor $\gamma_0$ for the IASW formation and the ion acceleration. Figure 13(b) shows the energies of 10

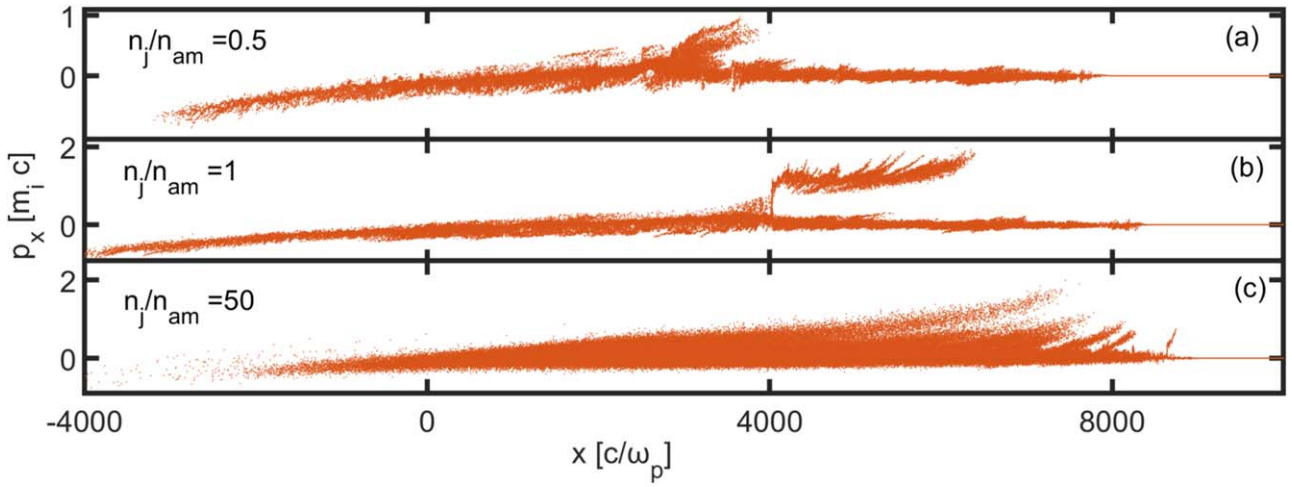


**Figure 10.** The longitudinal momentum distribution of the ions at the time $t = 9000\omega_p^{-1}$ for the different density ratios of the jet to the ambient plasma: (a) $n_j/n_{\rm am} = 0.5$, (b) $n_j/n_{\rm am} = 1$, and (c) $n_j/n_{\rm am} = 50$, respectively. The ion–electron mass ratio is artificially set as $m_i/m_e = 100$, and the initial jet Lorentz factor is fixed as $\gamma_0 = 15$.

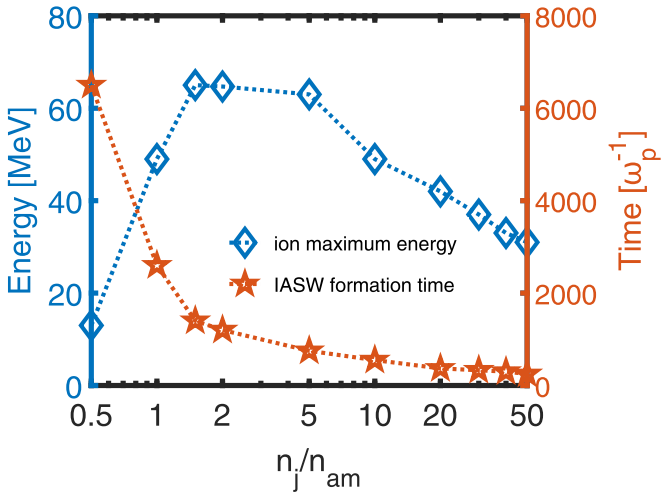


**Figure 11.** The maximum energy of the ions and IASW formation times as a function of the jet and ambient plasma density ratio $n_j/n_{\rm am}$. Other parameters are the same as those in Figure 10.

representative accelerated ions as functions of the coordinate. Since some ions may encounter more than one IASW, they will experience the acceleration or deceleration many times. A sudden increase (or decrease) in the ion energy indicates an encounter with the IASW. It is clear that some accelerated ions have encountered more than one IASW, for example, see the ion trajectories represented by thick red and blue lines in Figure 13(b).

We have also performed some additional simulations to investigate the effects of background magnetic fields on the IASW formation and ion acceleration in the interactions of pair jets with electron–ion plasmas. In simulations, a spatially uniform background magnetic field $B_0$ is assumed. The plasma magnetization is defined as $\sigma = (\omega_c/\omega_p)^2 = \epsilon_0 {B_0}^2/(m_e n_{am})$, where the Larmor frequency $\omega_c = eB_0/m_e$ and $\omega_p = (n_{\rm am} e^2/\epsilon_0 m_e)^{1/2}$ is the electron plasma frequency of the ambient plasma. Preliminary simulations show that the longitudinal magnetic field does not impact the IASW formation and ion acceleration. If the background magnetic field is transverse, however, it will play an important role in the IASW formation and ion acceleration. We find that the IASW may change from electrostatic to electromagnetic under a moderately transverse magnetic field ($\sigma = 10^{-2}$). A stronger magnetic field ($\sigma = 1$) can even inhibit the formation of the IASW. The effects of the magnetic field on the IASW formation and ion acceleration in the interactions of pair jets with electron–ion plasmas will be investigated in more detail in the future.

## 6. Conclusion and Discussion

In summary, we find that the ion acoustic shock wave (IASW) may be formed when an electron–positron ($e^-e^+$) jet is injected into an ambient electron–ion plasma, and the ions in the ambient plasma can be accelerated by the IASW consequently. The formation of the IASW has two stages. In the first stage, an IAW is induced due to the Buneman instability in the interaction of the injected jet with the ambient plasma. With the continuous increase of the IAW amplitude, the nonlinear effect will steepen the IAW and finally form the IASW in the second stage. The IASW moves forward, which may reflect some ambient ions in the upstream region and accelerate them to form a quasi-monoenergetic ion beam. For an initial $e^-e^+$ jet Lorentz factor $\gamma_0 = 100$ and an ion–electron mass ratio $m_i/m_e = 1836$, the maximum energy of the accelerated ions can reach about 580 MeV. For the sake of simplicity, this study is restricted to one-dimensional (1D) PIC simulations. The main difference in multidimensional simulations would be the emergence of transverse instabilities, such as the Weibel instability, filamentary instability, and oblique modes (Fried 1959; Weibel 1959; Bret et al. 2005, 2008, 2010). These transverse instabilities will also generate magnetic fields, and then the electrostatic IASW may evolve into electromagnetic shocks. This study may help us understand some related astrophysical processes, such as the fireball model of GRBs, the shock model of PWN, and the origin of high-energy cosmic rays (Drury 2012; Blasi 2013). With the advances in high-intensity laser technology, it has become possible to generate high-energy (MeV) charge-neutral $e^-e^+$ pair plasmas in the laboratory (Sarri et al. 2015; Chen et al. 2015; Liang et al. 2015; Warwick et al. 2017; Jiang et al. 2021; Peebles et al. 2021). Thus, our scheme will be attractive for experimental studies, which may open new opportunities for

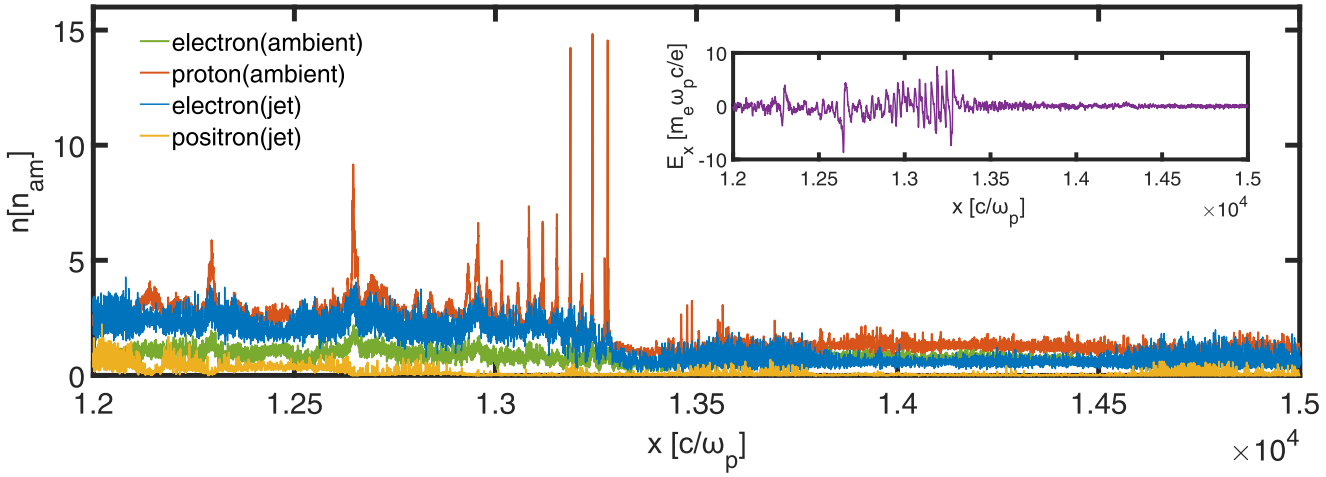


**Figure 12.** The density distributions of the $e^-e^+$ jet and ambient plasma at the simulation time $t = 40{,}000\omega_p^{-1}$, the subpanel shows the longitudinal electric field. The initial Lorentz factor of the $e^-e^+$ jet is $\gamma_0 = 100$, and the plasma density ratio of the $e^-e^+$ jet to the ambient plasma is $n_j/n_{\rm am} = 1$. A real ion–electron mass ratio $m_i/m_e = 1836$ is employed in this simulation.

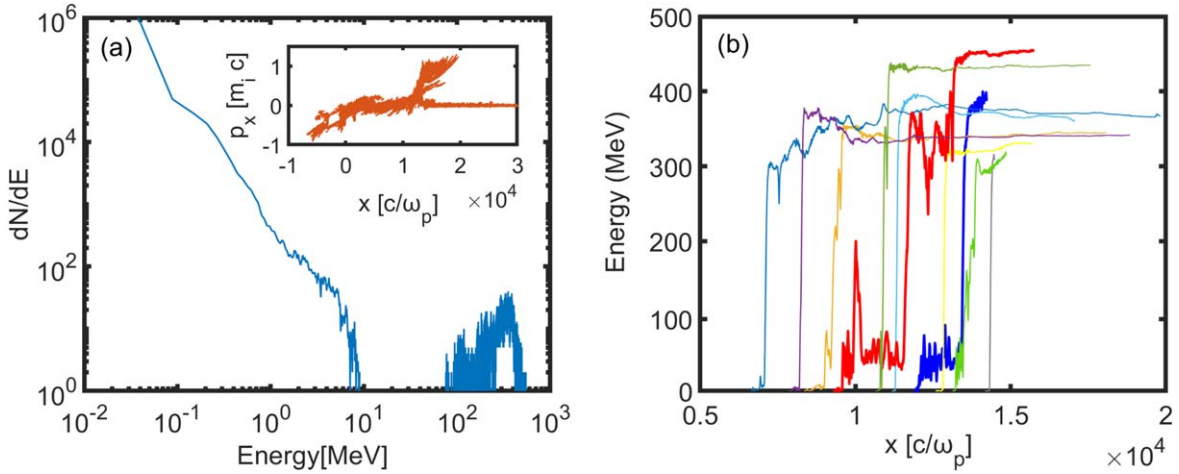


**Figure 13.** Left: ion energy spectrum in the upstream region $x \geqslant 14{,}000c/\omega_p$ at the time $t = 40{,}000\omega_p^{-1}$, the subpanel shows the longitudinal momentum distribution of the ions. Right: the energies of 10 representative accelerated ions as functions of the coordinate. All parameters are the same as those in Figure 12.

applications in astrophysics, plasma physics, and accelerator physics.

The work was supported by the National Natural Science Foundation of China (grant Nos. 11975154, 11675108, and 11721091), Science Challenge Project (No. TZ2018005), and Xinjiang Heaven Lake Hundred-Talent Program, and State Key Laboratory of Space Weather, CAS (grant No. SYS202107-04). The authors would like to acknowledge the OSIRIS Consortium, consisting of UCLA and IST (Lisbon, Portugal) for the use of OSIRIS. Simulations were performed on the Supercomputer at Shanghai Jiao Tong University.

## ORCID iDs

Jian Huang https://orcid.org/0000-0002-0190-6037
Su-Ming Weng https://orcid.org/0000-0001-7746-9462
Xin Wang https://orcid.org/0000-0003-0116-2573
Xing-Long Zhu https://orcid.org/0000-0002-5845-3139
Xiao-Feng Li https://orcid.org/0000-0002-7710-9800
Min Chen https://orcid.org/0000-0002-4290-9330
Masakatsu Murakami https://orcid.org/0000-0003-2220-7638
Zheng-Ming Sheng https://orcid.org/0000-0002-8823-9993

## References

Abeysekara, A. U., Albert, A., Alfaro, R., et al. 2018, Natur, 562, 82
Amato, E., & Arons, J. 2006, ApJ, 653, 325
Belloni, T. 2010, The Jet Paradigm, Vol. 794 (Berlin: Springer)
Blandford, R., Meier, D., & Readhead, A. 2019, ARA&A, 57, 467
Blandford, R. D., & Rees, M. J. 1974, MNRAS, 169, 395
Blasi, P. 2013, A&ARv, 21, 70
Bret, A., Firpo, M. C., & Deutsch, C. 2005, PhRvL, 94, 115002
Bret, A., Gremillet, L., Bénisti, D., & Lefebvre, E. 2008, PhRvL, 100, 205008
Bret, A., Gremillet, L., & Dieckmann, M. E. 2010, PhPl, 17, 120501
Buneman, O. 1958, PhRvL, 1, 8
Buneman, O. 1959, PhRv, 115, 503
Chen, F. F. 2016, Introduction to Plasma Physics and Controlled Fusion (Berlin: Springer)
Chen, H., Fiuza, F., Link, A., et al. 2015, PhRvL, 114, 215001
Cui, Y., Sheng, Z., Lu, Q., Li, Y., & Zhang, J. 2015, SCPMA, 58, 105201
Dieckmann, M. E., Ljung, P., Ynnerman, A., & McClements, K. G. 2000, PhPl, 7, 5171

Drury, L. O. C. 2012, APh, 39, 52
Fonseca, R. A., Silva, L. O., Tsung, F. S., et al. 2002, in Int. Conf. on Computational Science — ICCS 2002, ed. P. M. A. Sloot et al. (Berlin: Springer)
Forslund, D. W., Kindel, J. M., Lee, K., & Godfrey, B. B. 1979, PhFl, 22, 462
Fried, B. D. 1959, PhFl, 2, 337
Gallant, Y. A., Hoshino, M., Langdon, A. B., Arons, J., & Max, C. E. 1992, ApJ, 391, 73
Guo, J., & Yu, B. 2012, ChPhL, 29, 035203
Hirotani, K., Iguchi, S., Kimura, M., & Wajima, K. 2000, ApJ, 545, 100
Homan, D. C., Lister, M. L., Aller, H. D., Aller, M. F., & Wardle, J. F. C. 2009, ApJ, 696, 328
Hovatta, T., & Lindfors, E. 2019, NewAR, 87, 101541
Jiang, S., Link, A., Canning, D., et al. 2021, ApPhL, 118, 094101
Judice, C. N., Decker, J. F., & Stern, R. A. 1973, PhRvL, 30, 267
Kakad, A., & Kakad, B. 2016, PhPl, 23, 122101
Kakad, A., Omura, Y., & Kakad, B. 2013, PhPl, 20, 062103
Langdon, A. B., Arons, J., & Max, C. E. 1988, PhRvL, 61, 779
Lemoine, M., & Pelletier, G. 2011, MNRAS, 417, 1148
Liang, E., Clarke, T., Henderson, A., et al. 2015, NatSR, 5, 13968
Liu, M., Weng, S. M., Li, Y. T., et al. 2016, PhPl, 23, 113103
Liu, X., Cui, L., Luo, W. F., Shi, W. Z., & Song, H. G. 2007, A&A, 470, 97
Lotekar, A., Kakad, A., & Kakad, B. 2017, PhPl, 24, 102127
Loureiro, N. F., & Boldyrev, S. 2018, ApJL, 866, L14
Migliari, S., & Fender, R. P. 2006, MNRAS, 366, 79
Mirabel, I. F., & Rodríguez, L. F. 1999, ARA&A, 37, 409
Nishikawa, K., Mizuno, Y., Gómez, J. L., et al. 2020, MNRAS, 493, 2652
Nishikawa, K. I., Hardee, P., Richardson, G., et al. 2003, ApJ, 595, 555
Peebles, J. L., Fiksel, G., Edwards, M. R., et al. 2021, PhPl, 28, 074501
Perry, J. J., & Dyson, J. E. 1985, MNRAS, 213, 665
Piran, T. 2004, RvMP, 76, 1143
Plotnikov, I., Grassi, A., & Grech, M. 2018, MNRAS, 477, 5238
Plotnikov, I., & Sironi, L. 2019, MNRAS, 485, 3816
Polkas, M., Petropoulou, M., Vasilopoulos, G., et al. 2021, MNRAS, 505, 6103
Popel, S. I., Vladimirov, S. V., & Shukla, P. K. 1995, PhPl, 2, 716
Reynolds, C. S., Fabian, A. C., Celotti, A., & Rees, M. J. 1996, MNRAS, 283, 873
Romero, G. E., Boettcher, M., Markoff, S., & Tavecchio, F. 2017, SSRv, 207, 5
Rosenau, P. 1988, PhFl, 31, 1317
Russell, D. M., Russell, T. D., Miller-Jones, J. C. A., et al. 2013, ApJL, 768, L35
Saito, S., & Sakai, J.-I. 2004, PhPl, 11, 859
Sarri, G., Poder, K., Cole, J. M., et al. 2015, NatCo, 6, 6747
Scheuer, P. A. G. 1974, MNRAS, 166, 513
Shah, A., & Saeed, R. 2009, PhLA, 373, 4164
Sikora, M., & Madejski, G. 2000, ApJ, 534, 109
Sinha, U., Keitel, C. H., & Kumar, N. 2019, PhRvL, 122, 204801
Sinha, U., & Kumar, N. 2020, PhRvE, 101, 063204
Sironi, L., Plotnikov, I., Nättilä, J., & Beloborodov, A. M. 2021, PhRvL, 127, 035101
Sironi, L., & Spitkovsky, A. 2009, ApJ, 698, 1523
Sironi, L., Spitkovsky, A., & Arons, J. 2013, ApJ, 771, 54
Spitkovsky, A. 2008, ApJL, 682, L5
van der Swaluw, E., Achterberg, A., Gallant, Y. A., Downes, T. P., & Keppens, R. 2003, A&A, 397, 913
Wardle, J. F. C., Homan, D. C., Ojha, R., & Roberts, D. H. 1998, Natur, 395, 457
Warwick, J., Dzelzainis, T., Dieckmann, M. E., et al. 2017, PhRvL, 119, 185002
Waxman, E. 2006, PPCF, 48, B137
Weibel, E. S. 1959, PhRvL, 2, 83
Zhang, B. 2018, The Physics of Gamma-Ray Bursts (Cambridge: Cambridge Univ. Press)